PNAS RESEARCH ARTICLE | BIOPHYSICS AND COMPUTATIONAL BIOLOGY

Molecular mechanism of substrate transport by human peroxisomal ABCD3

Meghna Gupta[a,b,1], Nitesh Kumar Khandelwal[a,b], Devin J. Seka[a], Sree Ganesh Balasubramani[c], Miles Sasha Dickinson[b], Alexander Myasnikov[b], Ignacia Echeverria[c,d], and Robert M. Stroud[b,d,1]

Affiliations are included on p. 9.

Contributed by Robert Stroud; received June 13, 2025; accepted November 11, 2025; reviewed by Douglas C. Rees and Robert Tampé

ATP-binding cassette transporters of the D subfamily (ABCD1-3) mediate the export of CoA thioesters of fatty acids from the cytosol into peroxisomes for further oxidation. ABCD3 facilitates the transport of a broad spectrum of substrates, including branched-chain fatty acids, very long-chain fatty acids, bile salt intermediates, and dicarboxylic acids as CoA adducts. Mutations in ABCD3 are associated with defects in congenital bile acid synthesis. Despite its importance, the basis for substrate selectivity and the mechanism of transport by ABCD3 are not well defined. We report the cryogenic sample electron microscopy (cryo-EM) structures of full-length human ABCD3 in its apo state and bound to one of its physiological substrates (phytanoyl-CoA) at resolutions of 3.33 Å and 3.13 Å, respectively. Our biochemical assays reveal that substrate binding induces ATPase activity in ABCD3, suggesting a substrate-dependent conformational change. Structural comparison of the apo and substrate-bound states demonstrates that the substrate interaction brings nucleotide-binding domains closer together, providing a mechanistic basis of substrate-induced ATPase activity. These findings offer critical insights into the transport mechanism of ABCD3 and lay a structural foundation for understanding its role in peroxisomal metabolite import and related diseases.

ABC transporter | ABCD3 | structure | peroxisomes

Members of the ABCD1-3 family of ABC transporters transport export Coenzyme A (CoA) thioesters of fatty acids from the cytosol into peroxisomes for additional fatty acid oxidation (1). ABC transporters use the energy of ATP hydrolysis to transport substrates across the membrane (2–6). Of the four human ABC subfamily D transporters (7), ABCD1-3 are localized to the membrane of the peroxisome and are involved in export of acyl-CoA substrates from the cytosol into the peroxisome (8–10). Peroxisomes are small organelles present in all eukaryotic cells and play a key role in balancing oxidative stress, mediating α- and β- oxidation of fatty acids, synthesis of bile acids, catabolism of D-amino acids and polyamines, and biosynthesis of cholesterol, docosahexaenoic acid, and plasmalogens (11–14).

Human ABCD transporters generally function as homodimeric complexes, with each protomer consisting of a transmembrane domain (TMD) and a nucleotide-binding domain (NBD) (9). ABCD3 protein has 37.65 and 39.15% sequence identity with ABCD1 and ABCD2, respectively. ABCD1 and ABCD2 share 64.65% identity with each other and have an overlap in substrate preference, consisting of C18-C24 long-chain fatty-acyl CoAs (10, 14). ABCD3 is one of the most abundant proteins in the peroxisomal membrane and transports diverse substrates that include branched-chain fatty acids, very long chain fatty acids, bile salt intermediates- dihydroxycholestanoyl-CoA, and trihydroxycholestanoyl-CoA, dicarboxylic acids (15, 16). Loss or dysfunction of ABCD3 disrupts metabolic pathways, causing congenital bile acid synthesis defect 5, and liver abnormalities (17, 18). Alteration in expression levels of ABCD3 is associated with intrahepatic cholestasis, oculopharyngodistal myopathy, and its higher expression is correlated with better prognosis in various cancers (19–23).

Recently, Li et.al. found that expression levels of human ABCD3 in HEK293F cells were limiting. Noting the higher expression level of the homolog from *Caenorhabditis elegans* (PMP2) they expressed and determined the structure of a chimeric protein of the first 50 amino acids from PMP2 with the core domain of ABCD3 in substrate-bound and ATP-bound conformations (24). The structure of the full-length human ABCD3, particularly in the apo state, remained undetermined, reflecting a significant gap in our understanding. Structural insights into ABCD3 in its various conformational states are essential for elucidating the complete mechanism of its transport cycle and the conformational transitions it undergoes during substrate translocation.

Significance

Peroxisomes are involved in essential cellular metabolic processes that include fatty acid oxidation, bile acid synthesis, and detoxification. The ABCD subfamily of membrane transporter proteins transport fatty acyl-CoA molecules from the cytosol into peroxisomes. Among the ABCD subfamily members, ABCD3 transports branched-chain fatty acids and a range of other important metabolites. Dysfunction in ABCD3 has been associated with several inherited and acquired diseases. Using cryo-EM, we determined high-resolution structures of full-length human ABCD3 in both unbound and phytanoyl-CoA-bound forms. We show that substrate binding stimulates ATP hydrolysis activity by apposition of the two nucleotide-binding domains of ABCD3, adding structural insight into the mechanism of action of ABCD3 and its role in peroxisomal function and disease.

Author contributions: M.G., N.K.K., and R.M.S. designed research; M.G., N.K.K., D.J.S., S.G.B., I.E., and R.M.S. performed research; M.G., N.K.K., and R.M.S. contributed new reagents/analytic tools; M.G., N.K.K., D.J.S., S.G.B., M.S.D., A.M., I.E., and R.M.S. analyzed data; M.G. and R.M.S. funding acquisition; and M.G., N.K.K., D.J.S., S.G.B., I.E., and R.M.S. wrote the paper.

Reviewers: D.C.R., California Institute of Technology, Howard Hughes Medical Institute; and R.T., Goethe-Universität Frankfurt am Main.

The authors declare no competing interest.

[1]To whom correspondence may be addressed. Email: guptame@ohsu.edu or robertstroud111@gmail.com.

This article contains supporting information online at https://www.pnas.org/lookup/suppl/doi:10.1073/pnas.2513928122/-/DCSupplemental.

Published December 22, 2025.

In the present study, we determined structures of detergent-extracted human ABCD3 transporter using single-particle cryo-EM for the apo and substrate-bound states at 3.33 and 3.13 Å resolution. ATPase activity assays show that purified ABCD3 is active at a basal level and exhibits an increase in activity with substrates phytanoyl-CoA, or palmitoyl-CoA. Structural comparison between the apo and phytanoyl-CoA-bound states of ABCD3 shows that substrate binding promotes the dimerization of the nucleotide-binding domains (NBDs), providing a mechanistic explanation for the observed substrate-induced ATPase activity. In summary, our integrated approach using cryo-EM, biochemical assays, and atomistic molecular dynamics (MD) simulation provides a comprehensive view of substrate recognition and conformational transitions, delineating key steps in the transport cycle of the peroxisomal fatty acyl-CoA transporter—human ABCD3.

Results

Biochemical Characterization and Structure Determination of Human ABCD3. Human ABCD3 is a homodimer of ~75 kDa. subunits, each half transporter having six transmembrane helices (TMHs) and one nucleotide binding domain (NBD). It is a half transporter like other ABCD subfamily ABC transporters and must form a dimer to function. Purification of full-length human peroxisomal ABC transporters has been challenging, and other approaches resorted to using a chimeric version of the protein (24, 25). We cloned the full-length human ABCD3 (hABCD3) and expressed it in *Sf9* cells. We successfully purified hABCD3 with high purity and obtained an amount adequate for structural and biochemical characterization (Fig. 1*A*). We tested the functionality of detergent extracted and purified hABCD3 protein using ATPase assay and found it is active. The ATPase activity of hABCD3 is induced ~5-fold in the presence of its substrates phytanoyl-CoA, or palmitoyl-CoA (Fig. 1*B*).

For structural analysis, we prepared cryo-EM grids with hABCD3 samples and collected and processed cryo-EM data. The apo hABCD3 structure was determined to be 3.3 Å resolution (Fig. 1 *D*–*F* and *SI Appendix*, Fig. S1) and was in an inward open conformation similar to the human ABCD1 transporter structures (25–28). The substrate-bound structure was also inward-facing as found for the chimeric structure (24), but with the NBDs closer together relative to the apo-structure. The overall density map was sufficient to model all six TMHs and NBD in both protomers (*SI Appendix*, Fig. S2) and showed that hABCD3 assembles as a twofold symmetric homodimer. The hABCD3 TMHs are arranged in type IV ABC transporter topology where two TMDs of each monomer, TMH 4 and 5, are domain swapped across the interface of the two halves (Fig. 1*C*) to bundle with TMH 1, 2, 3, and 6 of the other protomer (Fig. 1 *D* and *F*) (6, 29). In this arrangement, the intracellular loop (ICL) between TMH4 and 5 of one protomer is sandwiched between TMHs and the NBD of the second protomer (Fig. 1 *D* and *F*).

Phytanoyl-CoA Binding to Human ABCD3. Phytanoyl-CoA is a known substrate of hABCD3 whose transport from the cytosol into peroxisomes is essential for the α-oxidation of phytanic acid (30). We determined the binding affinity of phytanoyl-CoA to

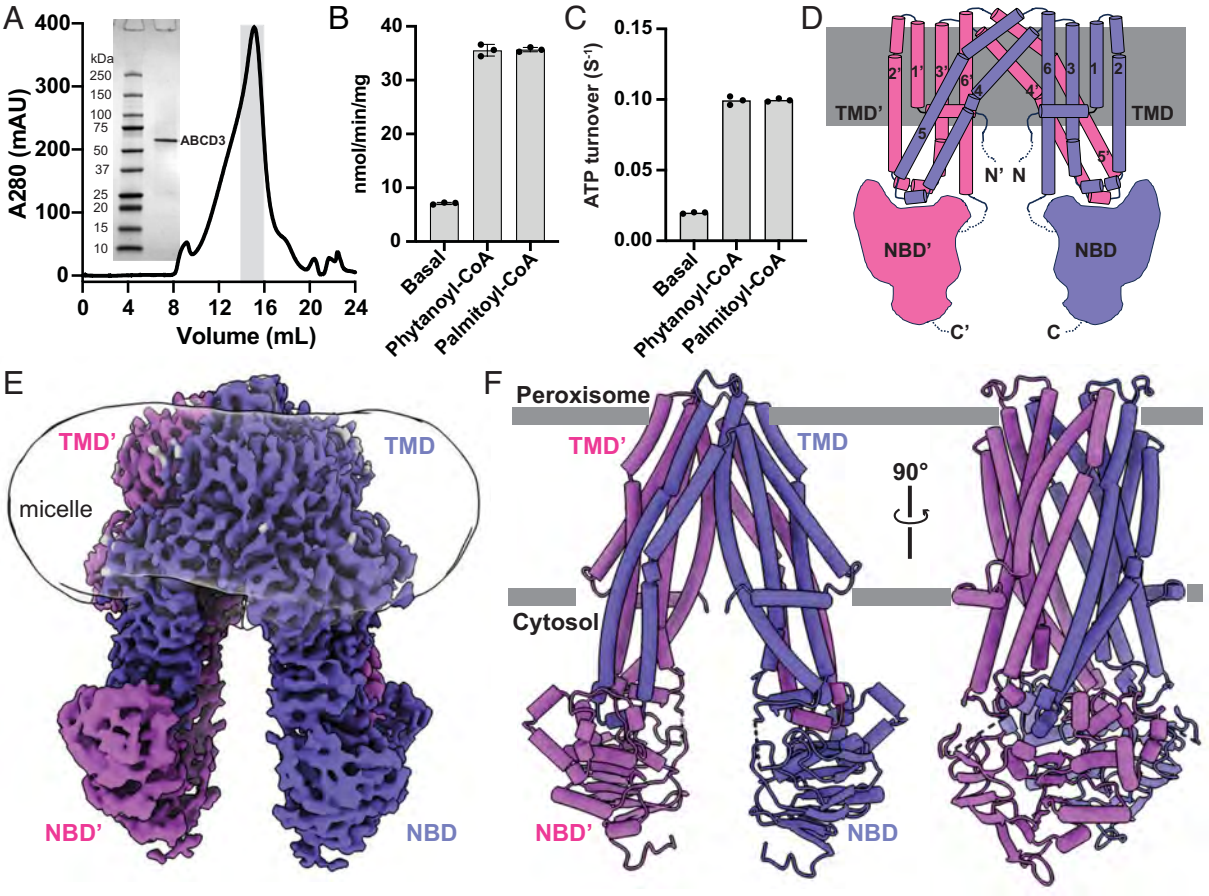

Fig. 1. Human ABCD3 overall structure. (*A*) Size-exclusion chromatography profile of purified hABCD3 and SDS gel of peak fraction. (*B*) ATPase activity of ABCD3 at basal level and in the presence of its substrates (phytanoyl-CoA and palmitoyl-CoA). (*C*) ATPase turnover of ABCD3 at basal and in the presence of substrates. (*D*) Overall topology of ABCD3. (*E*) Cryo-EM map of ABCD3 as a homodimer in GDN detergent (dark green representing protomer A and light green representing protomer B). (*F*) Model of ABCD3 with color theme as shown in (*E*).

ABCD3 using microscale thermophoresis (MST) as 33 ± 5 μM (Fig. 2*A*). To determine the structural basis of this interaction, we prepared a complex of hABCD3 with phytanoyl-CoA for cryo-EM structure determination. The structure, resolved to a higher resolution of 3.1 Å. (*SI Appendix*, Figs. S3 and S4) versus the apo state (3.3 Å) (*SI Appendix*, Figs. S1 and S2) reveals two phytanoyl-CoA molecules symmetrically bound to the ABCD3 homodimer (Fig. 2 *B* and *C*).

Phytanoyl-CoA is composed of hydrophilic coenzyme A and hydrophobic phytanic acid. Within the ABCD3 protein, it adopts a V-shaped conformation where coenzyme A is buried within the substrate binding pocket surrounded by transmembrane domains (Fig. 2 *D*, *Right* panel). The adenine ring CoA is bound by specific hydrogen bonds from the side chains of E111' (TMH1'), Y330 (TMH5), Y357 (TMH6) to N1, N10 of the adenine base (Fig. 2*D*). The 3 phosphate anions remain solvated in the cytosolic entry cavity with positive charges from the eN of K322(TMH5) with possible ionic interaction and nearby positive charges in the cavity from R366, R373, R366', and R373'. The 2' hydroxyl of the ribose ring makes hydrogen bonds with T326 (TMH5). The 3'-phosphate is close to K322. The oxygen of the first phosphate from the 5' diphosphate interacts with S368 (TMH6) (Fig. 2 *D*, *Lower Right* panel). Two glycine residues G241(TMH4) and G372 (TMH6) flank the pantothenic part of CoA allowing access of the phytanoyl chain to the bilayer (Fig. 2*D*). The phytanoyl branched chain lies in a hydrophobic groove on the outside of the protein in between TMHs 3-6 of one protomer and TMH1' of the adjacent protomer (Fig. 2 *C* and *D*). The groove is composed of sidechains from TMH3 (F219, I218, V215, I214, F211), TMH4 (M234, V238, L242), and TMH6 (L371, I374, V375) (Fig. 2 *D*, *Left* panel).

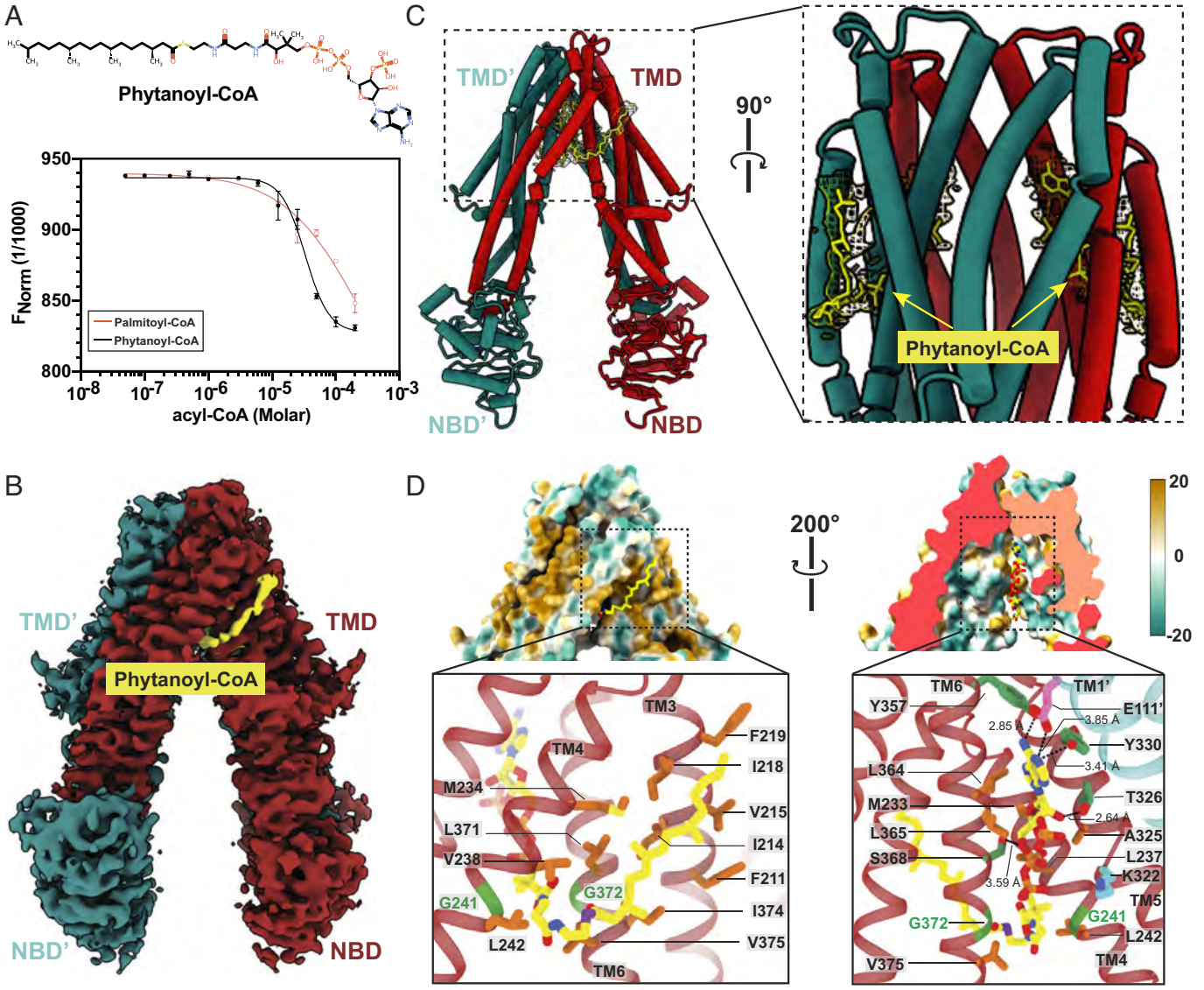

Fig. 2. Phytanoyl-CoA bound Human ABCD3. (*A*) The binding of phytanoyl-CoA (EC_{50}= 33 ± 5 μM) and palmitoyl-CoA (EC_{50}= 279 ± 6 μM) using MST data with error bars representing SD (n = 3) were used to extract the Hill coefficient for binding as ~2.33 (*B*) Cryo-EM map of phytanoyl-CoA bound ABCD3. Density corresponds to phytanoyl-CoA is colored yellow, protomer A red and protomer B teal. (*C*) Model of phytanoyl-CoA bound ABCD3 with color code as in (*B*). The density corresponding to the phytanoyl-CoA is shown in mesh. *Left* panel showing the view as *B*, *Middle* panel rotation of *Left* panel by 90° about the vertical axis. (*D*) Hydrophobic surface of ABCD3 around the bound phytanoyl chain with annotated hydrophobic interactions in the *Lower Left* panel. The sectioned view of bound phytanoyl-CoA bound (*Upper Right* panel) annotated interactions in the *Lower Right* panel. Phytanoyl-CoA is colored yellow, glycines flanking the cavity are teal, hydrophobic residues are orange, polar-uncharged residues green, negatively charged residues pink, and positively charged amino residues cyan; colored by atom- oxygen (red), nitrogen (blue), and sulfur (violet).

Molecular Dynamics Simulation Reveals Phytanoyl-CoA Interacting Residues. Phytanoyl-CoA is a large amphipathic substrate with distinct hydrophilic and hydrophobic moieties. We performed molecular dynamics (MD) simulations to track the interactions and conformational changes of phytanoyl-CoA within the ABCD3 substrate binding cavity, specifically investigating how its molecular size and amphipathicity influence dynamic behavior over time. An initial 50 ns equilibration was conducted with the ligand bound to the protein supported in a 1-palmitoyl-2-oleoyl-sn-glycero-3-phosphocholine (POPC) lipid bilayer membrane. Subsequently, three independent 500 ns. production runs were generated to enhance conformational sampling, each initiated from a distinct starting configuration (Fig. 3 and *SI Appendix*, Fig. S5). During the simulation time across all three trajectories, phytanoyl-CoA remained within the cavity; however, it displayed significant conformational flexibility and variable interaction patterns with different protein residues. We expect the long, hydrophobic lipid tail of phytanoyl-CoA, which is located outside the protein cavity (Fig. 2*D*), to be flexible.

We focused on the CoA moiety of phytanoyl-CoA, which resides within the ABCD3 cavity. This moiety was divided into five parts (adenine ring, ribose-3-phosphate, diphosphate, pantothenate, and cysteamine) to examine the movement of the center of mass for each part individually (Fig. 3 *A* and *B*). The adenine ring, pantothenate, and cysteamine near the exit point from the ABCD3 cavity show greater movement than the central (ribose-3-phosphate, 5-diphosphate). This is indicated by the deviations based on the movement of the center of masses from their initial positions (Fig. 3*B*). This flexibility leads to new interactions with nearby residues in the substrate binding cavity of ABCD3 (Fig. 3*D*). Specifically, phytanoyl-CoA in protomer A interacts with residues R373, R371, Q369, and K322 of protomer A, as well as R366' and R373' of protomer B within the cavity.

Substrate-Induced Changes in Human ABCD3. The apo and phytanoylCoA bound structures are in inward-facing open states with rmsd (RMSD) of 1.36 Å between their respective Cα positions (Fig. 4). The phytanoyl-CoA interaction with ABCD3

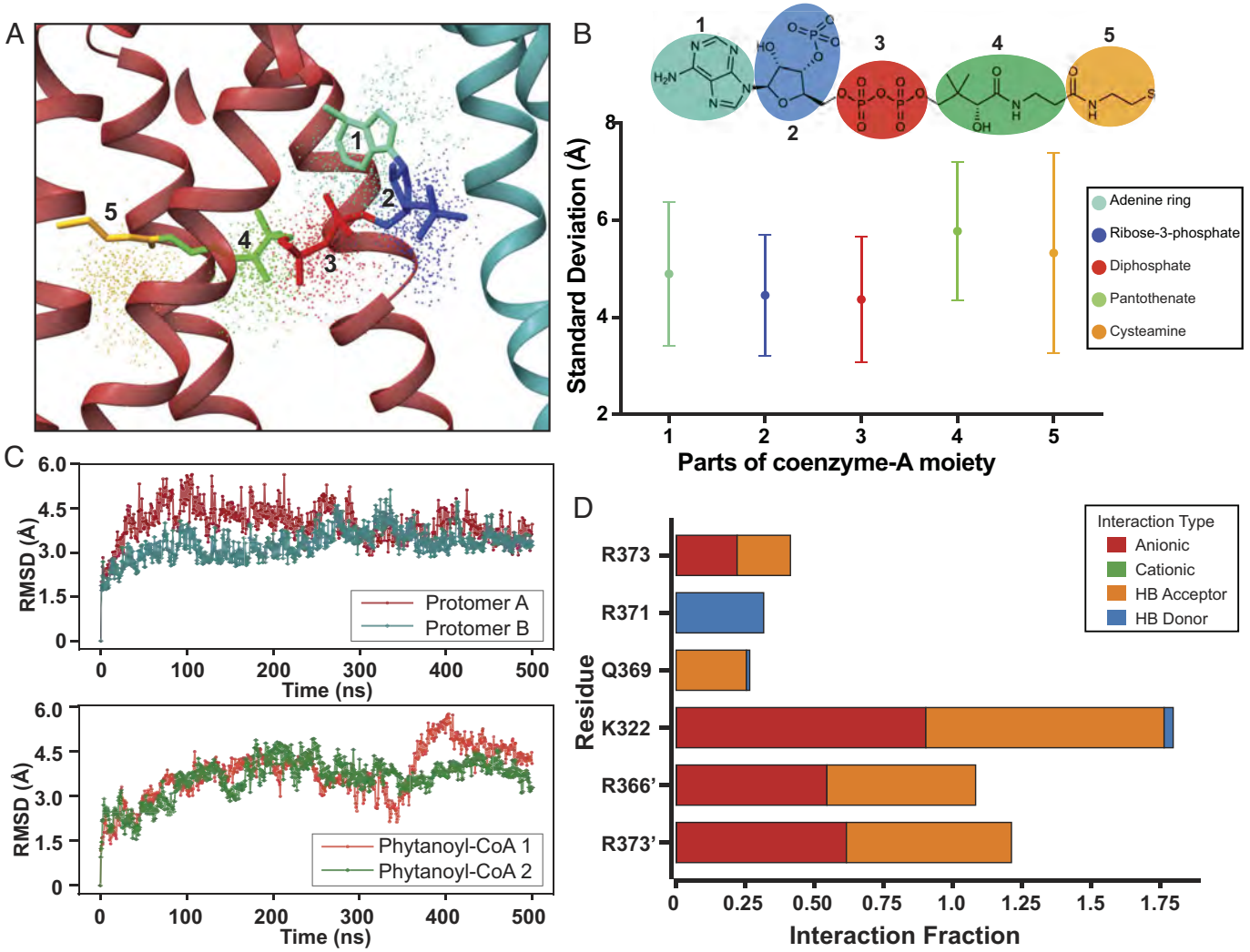

Fig. 3. Molecular dynamics simulation of phytanoyl-CoA bound to hABCD3. (*A*) Structure and dynamics of phytanoyl-CoA 1 within the dimer cavity. Its final conformation (sticks) is shown, segmented into adenine (Turquoise), ribose-3-P (Blue), diphosphate (Red), pantothenate (Green), and cysteamine (Yellow). Correspondingly colored points illustrate the spatial volume explored by the center of mass (COM) for each segment during a representative trajectory. (*B*) Segmental flexibility of phytanoyl-CoA 1. The SD of COM displacement quantifies the positional fluctuation for each segment (colors as in *A*). Larger SD values for the terminal adenine and cysteamine segments highlight their greater conformational flexibility. (*C*) System stability assessed by RMSD relative to the initial structure, shown for a representative trajectory. *Top*: Protein backbone Cα RMSD for Protomer A (brown) and B (teal). *Bottom*: Heavy atom RMSD for phytanoyl-CoA 1 (orange) and 2 (green). (*D*) Persistent substrate–protein interactions identifying key binding residues. Interaction fractions (% time) depict significant hydrogen bonds and ionic contacts between phytanoyl-CoA 1 and residues from Protomer A and B′ (prime denotes Protomer B). Displayed interactions represent consistent contacts, maintained for ≥10% of the time across all three replicate simulations.

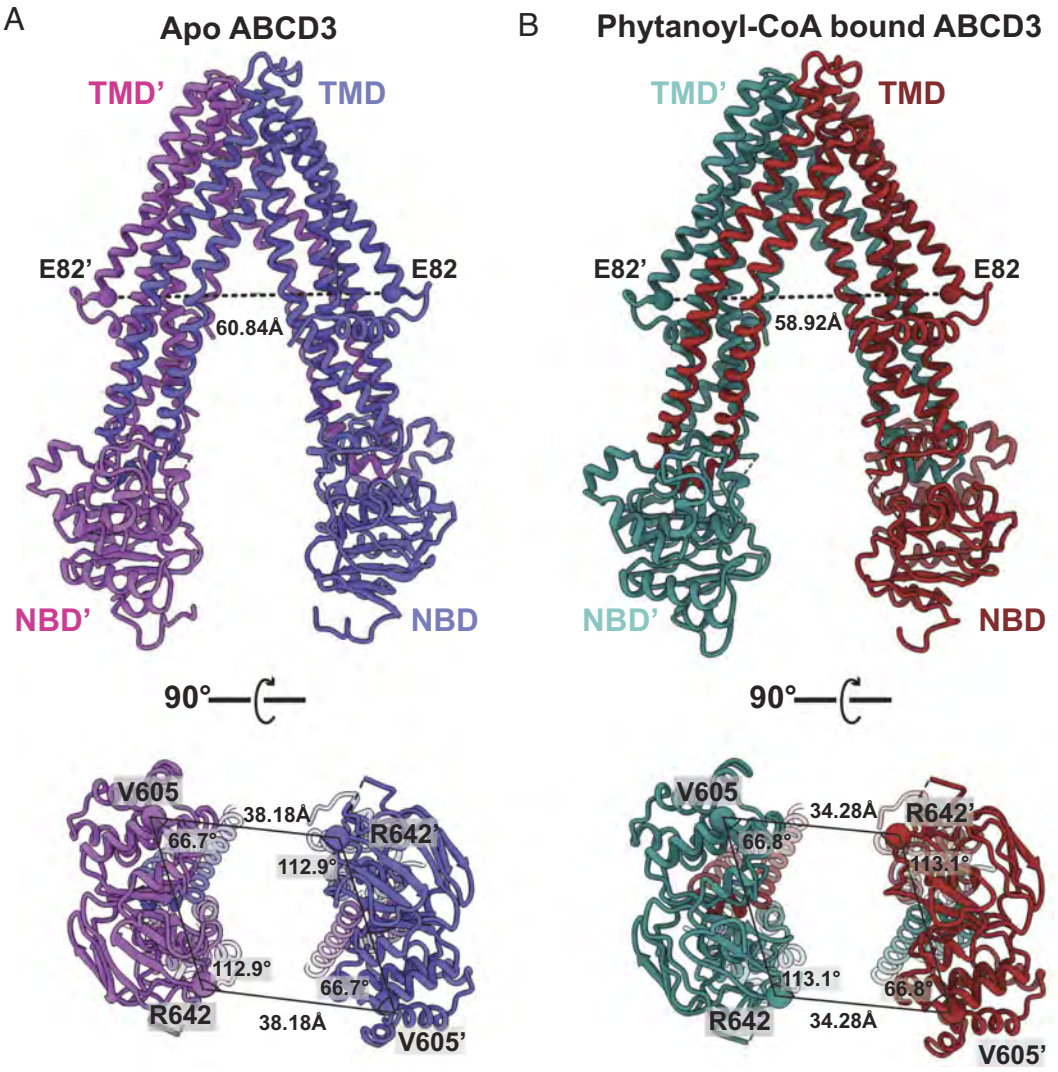

Fig. 4. Phytanoyl-CoA binding induced changes in ABCD3. (*A*) Distance between TMDs and NBDs and angles between protomers in the apo state (*B*) Phytanoyl-CoA bound state. Change is measured as distance between E82 and E'82 residues in TMH 1 of ABCD3 protomers (*A*) in apo state (*Top* panel) to (*B*) in phytanoyl-CoA bound state (*Top* panel). The change of NBD positions measured as angles and distance between V605 and R642' of NBDs from each protomer of ABCD3 (*A*) in apo state (*Lower* panel) to (*B*) in phytanoyl-CoA bound state (*Lower* panel).

brings the TMD of each half closer together such that the distance between E82s of TMH1 from both protomers is reduced from 60.8 to 58.9 Å. This translates to larger movement between the NBDs. The distance between V605 from NBD and R642' from NBD' reduced from 38.2 Å (Fig. 4*A*) to 34.3 Å (Fig. 4*B*).

Phytanoyl-CoA interacts with TMH 3, 4, 5, 6 of one protomer and TMH1' of the second protomer. TMH4 and 5 are closer to the binding cavity (Fig. 5*A*). This movement reduces the distance between the bound phytanoyl-CoA position and ABCD3 residues (Fig. 5*B*). For the residues that make hydrogen bonds with the CoA moiety, [Y330 (TMH5), T326 (TMH5), Y357 (TMH6), S368 (TMH6)] distances lie in the range of 4.1 to 5.5 Å (Fig. 5 *B*, *Upper* panel) and reduce to 2.6 to 3.6 Å in the phytanoyl-CoA bound structure (Fig. 5 *B*, *Lower* panel).

Attempts to Obtain an Outward-Facing Conformation. To determine the structure of ATP-trapped states, we generated an ATP hydrolysis-deficient mutant (E596Q) of a conserved glutamate in the Walker B motif of WT ABCD3 and determined structures in the presence of ATP. We also determined structures with wild-type ABCD3 in the presence of AMP-PNP or ADP-vanadate. In all cases, the structures were close to the inward open conformations we report here. This is in contrast to the structures of chimeric ABCD3 that brought the NBDs together and resulted in an outward open state (24). Evidently, the chimeric protein more readily binds ATP, or more readily undergoes the transition to an outward open state upon binding ATP. We also attempted reconstitution into nanodiscs both after elution from affinity chromatography beads and directly on-bead as we used previously (31, 32) but found this unworkable with our current preparation in LMNG, perhaps because of its low critical micellar concentration.

Discussion

Overexpressing full-length human peroxisomal ABCD subfamily transporters (ABCD1–D3) has proven challenging, with several studies reporting insufficient yields of recombinant proteins for structural analysis. We successfully expressed and purified full-length human ABCD3 (hABCD3) from insect Sf9 cells. ATPase activity measurements confirmed that the purified protein was active and exhibited phytanoyl-CoA and palmitoyl-CoA induced ATPase activity (Fig. 1*B*). Our observed basal ATPase activity was low, which subsequently increased ~5-fold upon introduction of

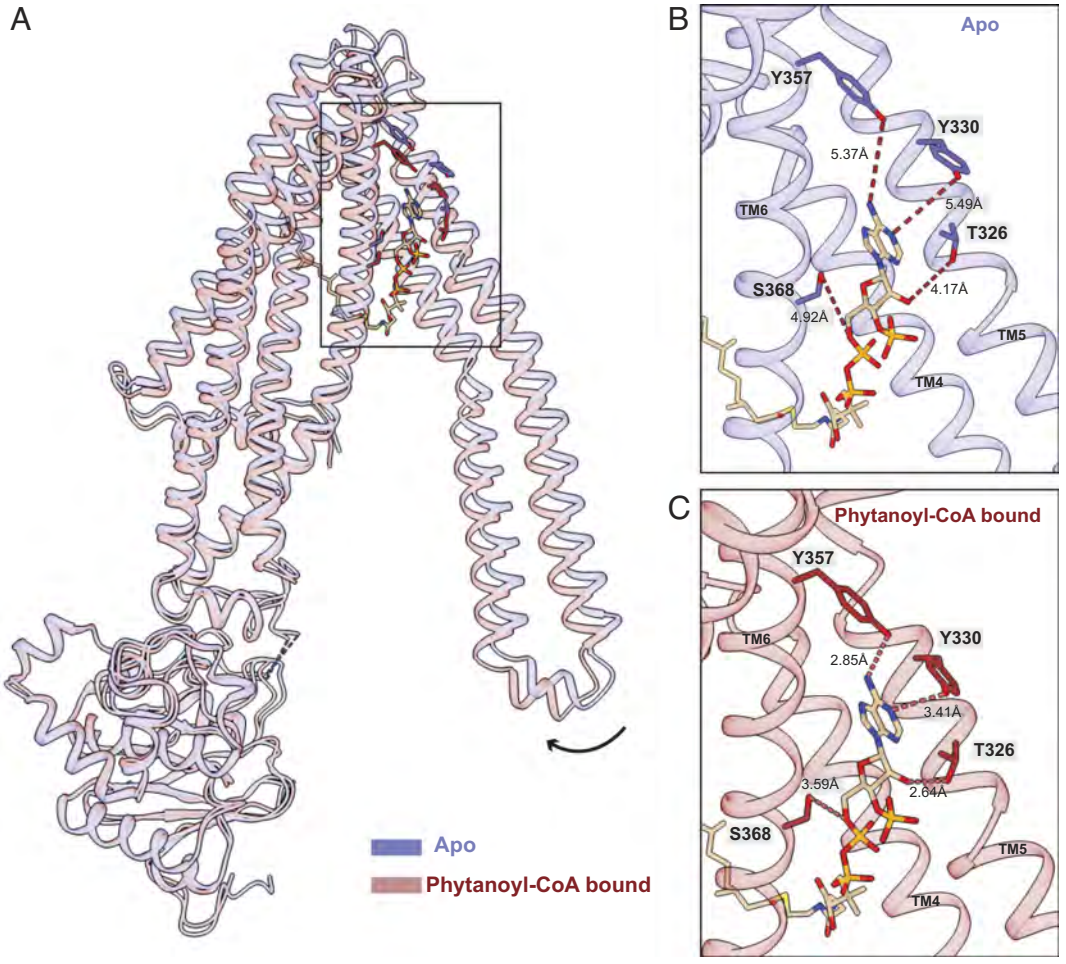

Fig. 5. Comparison of apo and phytanoyl-CoA bound ABCD3 protomer. (*A*) Comparison of the transmembrane helices of apo and phytanoyl-CoA bound protomer A obtained from superimposition of the NBD region. In the phytanoyl-CoA bound state, TMH 4 and 5 rotate and move inward. (*B*) In the apo state TMH 4 and 5, the distances between residues (Y330, T326, of TM5 and Y357, S368 of TM6) and the position of phytanoyl-CoA in the bound structure (*Upper* panel) decrease on binding phytanoyl-CoA as in panel (*C*).

its physiological substrates, demonstrating substrate-dependent ATP hydrolysis. Similar observations were made by Chen et al. in the case of another ABCD subfamily transporter (ABCD1) where the basal ATPase activity was very low and increased in the presence of C22:0-CoA (25). In another study on ABCD1 (33), Jia et al., report ~180 fold higher level of ATPase activity than Chen et al. The major difference between these assays was that Chen et al. used a chimeric ABCD1 in which the first 63 amino acids at N-terminal of human ABCD1 were replaced by 65 amino acids of *C. elegans* PMP-4, while Jia et al. used N-terminal truncated ABCD1 (54N-terminal residues deleted). In the same year, Le et al. reported specific ATPase activity of full-length ABCD1 in presence of different substrates in the range of ~20 nmol/mg/min (26). This is comparable with the ATPase activity of full-length human ABCD3 in the presence of substrates we report here. However, the full-length ABCD1 ATPase activity reported by Le et al. is very low in comparison to chimeric ABCD1 (25) or truncated ABCD1 (33).

In the case of ABCD3, higher ATPase activity was observed in chimeric ABCD3 (24). We reason that the N-terminal ~50 amino acids of human ABCD family members may play a regulatory role in ATPase activity, hence replacing it with the *C. elegans* PMP4 sequence or deleting it resulted in elevated ATPase activity. This is supported by a recent publication where ATPase activity in the case of the N-terminal truncated (54 residues) was higher than for full-length ABCD1 (28).

In our phytanoyl-CoA-bound structure, two additional densities correspond to phytanoyl-CoA. The MST-based interaction analysis between ABCD3 and phytanoyl-CoA revealed a Hill coefficient of ~2.33, indicating strongly positive cooperative binding. This interaction brings the two halves of ABCD3 closer together, leading to a reduced distance between the NBDs (Fig. 4). The substrate-dependent narrowing of the NBD positions may facilitate dimerization upon ATP binding, potentially explaining the enhanced ATPase activity observed in the presence of substrates (Fig. 1*B*).

Substrates for ABCD family transporters are predominantly long fatty acid chain–containing molecules. The flexible nature of these substrates facilitates interaction with different residues during the transport cycle. We compared substrate binding of phytanoyl-CoA-bound to ABCD3 with oleoyl-CoA binding to ABCD1 (27), and with C22:0-CoA bound to ABCD1 (25) (*SI Appendix*, Fig. S6). The CoA moiety of oleoyl-CoA in the ABCD1 transporter pocket occupies a similar site to that of CoA in phytanoyl-CoA-bound ABCD3 (*SI Appendix*, Fig. S6*A*) though the fatty acid chains lie in different grooves on the hydrophobic surface of the transmembrane region. Superimposition of phytanoyl-CoA-bound ABCD3 with C22:0-CoA ABCD1 shows that the substrates occupy different positions (*SI Appendix*, Fig. S6*B*). While the phytanoyl chain lies on the surface of one monomer, the C22:0-CoA fatty acid chain interaction extends from one TMD across to the other TMD′ (*SI Appendix*, Fig. S6*B*).

In ABCD1, for both oleoyl-CoA and C22:0-CoA, the fatty-acyl chain lies between the TMDs structure with C26:0-CoA, the fatty-acyl chain present outside of the TMDs as in our substrate-bound ABCD3 (28), while in phytanoyl-CoA-bound ABCD3, it reaches the lipid surface of the TMDs. One possibility justifying the differences in substrate-binding is that these structures represent distinct stages of the transport cycle. It is likely that the substrate-bound conformation of ABCD1 represents a later stage in the transport cycle than the currently observed phytanoyl-CoA-bound state of ABCD3. In that later stage, the CoA moiety is rotated and oriented toward the cytosol, while the acyl chain is oriented to the outside, more deeply embedded between transmembrane helices, potentially bridging the two transmembrane domains (TMDs). This complete substrate engagement may induce conformational changes in ABCD3 that promote ATP binding and drive further repositioning of the CoA moiety toward the cytosolic side. A similar observation for substrate movement involves a flipping mechanism, which has been observed in other ABC transporters such as TmrAB (34), MsbA (35), and PglK (36). TmrAB, for example, is a heterodimeric ABC transporter implicated in the translocation of lipid A precursors (34). Likewise, MsbA functions as a lipid A floppase (37, 38). In both cases, clusters of positively charged residues within the substrate-binding cavity are thought to interact with the phosphate groups of their substrates. Analogously, the substrate-binding cavity in ABCD3 contains positively charged residues that interact with CoA-moiety. During the transition to the outward-facing conformation, the substrate may undergo a rotational movement of the polar component that translocates the acyl chains toward the outside (flopping), which facilitates substrate release upon ATP binding and hydrolysis. A chimeric ABCD3 protein structure with phytanoyl-CoA bound was published during our manuscript preparation and revealed an inward-facing state (24). Our full-length structure is very similar to that structure with an RMSD of 0.973 Å between 567 Cα atoms, with a slight difference in the binding poses of phytanoyl-CoA (*SI Appendix*, Fig. S7).

Structural analysis of ABCD3 in two distinct states (apo and substrate-bound), together with previously published ATP-bound states (24), lead us to propose a model for ABCD3-mediated phytanoyl-CoA transport (Fig. 6). In its resting state, ABCD3 exhibits an inward-facing conformation where the two nucleotide-binding domains (NBDs) remain apart. Upon cooperative substrate binding, the TMDs move closer together, forming a narrower inward-facing transport cavity. In ABCD3, as in TmrAB substrate binding occurs in an inward open state (34). In ABCD3, substrate binding brings the TMDs closer together (Fig. 4) mostly by movement of TM4, 5, the upper half of TM6 and the NBDs (*SI Appendix*, Fig. S8). In TmrAB, this conformational change is mediated by TM6 from both TmrA and TmrB (34). In ABCD3, apo (wide) to substrate-bound (narrow)

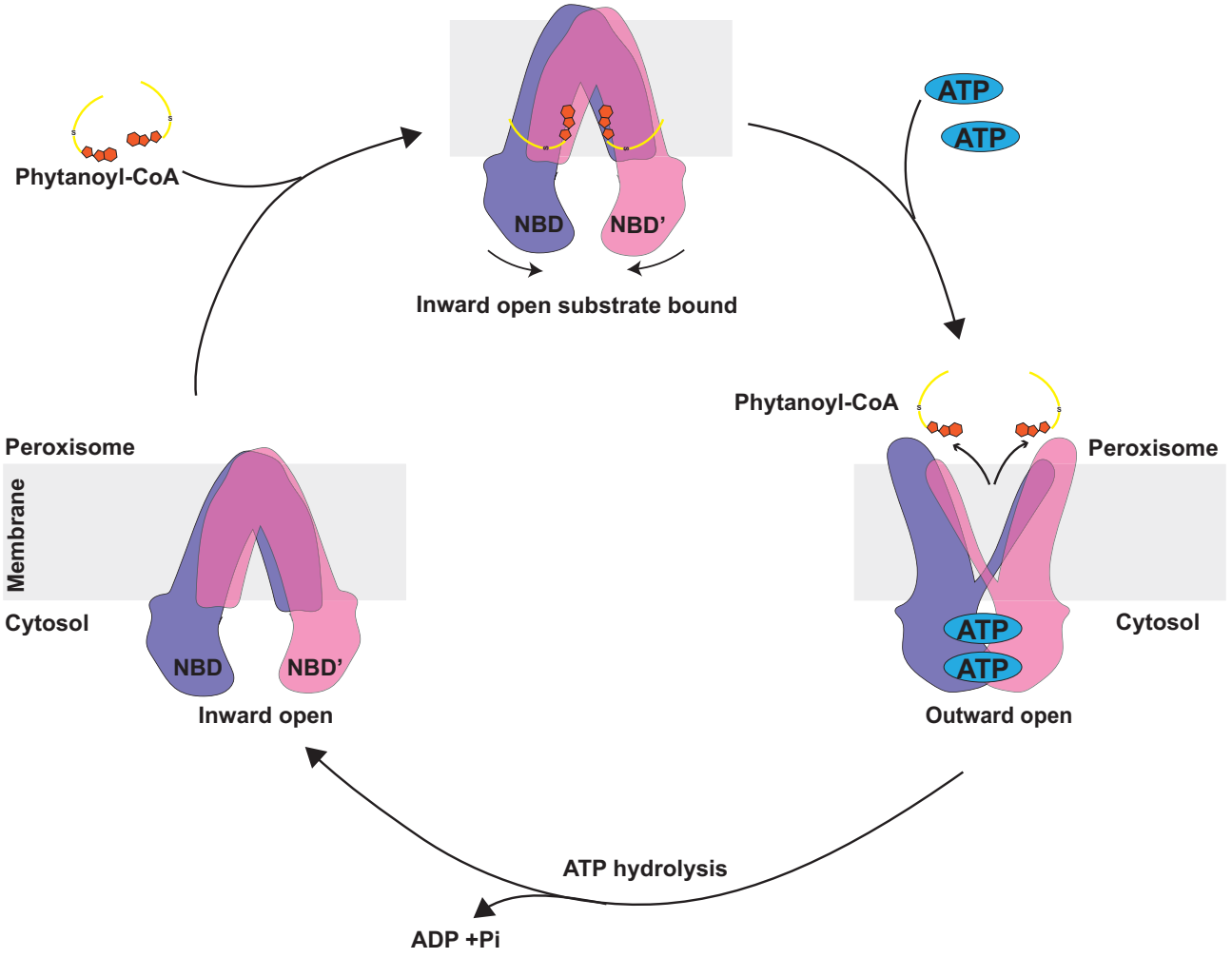

Fig. 6. Proposed model of the transport cycle of ABCD3. Substrate (phytanoyl-CoA) binds to inward-open state of ABCD3 and brings NBDs closer together. ATP binding brings NBDs further together resulting in an outward-open state (PDBID:8Z0F) (24). In this state, substrate-release to the peroxisome would be as an intact molecule. Finally, the hydrolysis of ATP resets the transporter to an inward open apo state.

conformation change causes a decrease in the inter-NBD distance of ~4Å (Fig. 4). This conformational change may facilitate the dimerization of the NBDs upon ATP binding, transitioning ABCD3 to an outward-facing conformation. The shift from inward-facing to outward-facing conformation would enable release of phytanoyl-CoA across the membrane completing the transport process. ATP hydrolysis and subsequent phosphate release would trigger conformational changes that reset ABCD3 to its resting state for another transport cycle (39, 40).

Materials and Methods

Human ABCD3 Expression and Purification. The human ABCD3 (Uniprot ID: P28288) gene was synthesized by Genscript and cloned in pFastBac1 vector with a C-terminal 8xHis tag for baculovirus-mediated expression in *Spodoptera frugiperda* cell line *Sf9*. Bac-to-Bac™ Baculovirus Expression System (Thermo Fisher Scientific) protocols were followed to prepare recombinant baculovirus. Baculovirus multiplicity of infection (MOI) of 2 was used to infect the *Sf9* cells and cultured for 48 h at 27 °C. The cells were harvested by centrifugation and then resuspended in the Lysis buffer (50 mM Tris Cl, pH 7.5, 100 mM NaCl, 10 mM $MgCl_2$, 10% glycerol) supplemented with 1X EDTA-free complete protease inhibitor cocktail tablets (Sigma-Aldrich). Cells were lysed using sonication at 4 °C and then Dounce homogenized. Then, 1% w/v lauryl maltose neopentyl glycol (LMNG) (Anatrace): 0.1% w/v cholesteryl hemisuccinate (CHS) (Anatrace) was added to the lysate to solubilize the membrane fraction overnight. Solubilized membrane was separated by centrifugation at 104,630×*g* for 30 min. Further, 5 mM imidazole was added to the supernatant. HisPur™ Cobalt Resin (Thermo Fisher Scientific) was equilibrated with the Lysis buffer and 5 mM imidazole, and the protein in the supernatant was allowed to bind for 2 h on a shaking platform. The mixture was passed through a disposable gravity column and flow-through was collected. The resin was washed with 10 mM imidazole, 0.02% w/v glyco-diosgenin (GDN) (Anatrace) containing lysis buffer. ABCD3 was eluted from the cobalt resin with 150 mM imidazole, 0.02% GDN w/v containing lysis buffer. The protein was concentrated with Amicon Ultra-15 centrifugal filters (MilliporeSigma) and further purified using size exclusion chromatography (SEC) in SEC buffer (25 mM HEPES pH 7.5, 100 mM NaCl, 2 mM $MgCl_2$, and 0.02% w/v GDN). 0.02% w/v GDN was used throughout the protocol to optimize cryoEM imaging. For ligand binding and activity assays 0.005%:0.0005% w/v LMNG:CHS was used.

ATPase Activity Assay. ATPase assays were performed using the malachite green based colorimetric ATPase/GTPase Activity Assay Kit (Sigma-Aldrich). The, 4 μg of purified ABCD3 in buffer 25 mM HEPES pH 7.5, 50 mM KCl, 0.005%:0.0005% LMNG:CHS was used to assess ATPase activity in a 40 μL reaction volume in triplicates. The reaction mixture above with 2 mM ATP/Mg^{2+} with or without substrate was incubated for 30 min at 37 °C. The substrates phytanoyl-CoA and palmitoyl-CoA (Avanti Polar Lipids) when mentioned were added at 250 μM. The reaction was stopped by adding reagent from the assay kit and incubated for 30 min at room temperature. The colorimetric product corresponding to phosphate released was assessed by measuring absorbance at 620 mm using Tecan Spark® Multimode Microplate Reader. The ATPase turnover values for ABCD3 were calculated using the Michaelis–Menten equation Y = Et**kcat**X/(Km + X) in GraphPad Prism version 10.4.1, with fixed constraints of 2 mM ATP, Km = 150.3 μM, and 0.65 μM protein concentration.

Cryo-EM Sample Preparation. For the apo structure determination, ABCD3 was used at ~6 mg/mL. Then, 3.5 μL of the sample was applied to Quantifoil R 1.2/1.3 300-mesh Au holey carbon grids. Fluorinated Fos-Choline-8 (Anatrace) at a final concentration of 1.5 mM was added directly on the grid and mixed with the sample. Mark IV Vitrobot (FEI) was used for sample vitrification on the grids at 8 °C and 100% humidity. A blot force of −2 and blotting time between 3 and 7 s was used to remove excess sample from the grids. The grids were rapidly plunge frozen after blotting in liquid ethane and stored in liquid nitrogen.

For the substrate-bound structure, 0.5 mM phytanoyl-CoA was added to ABCD3 at a final concentration of ~8 mg/mL. Then, 3.5 μL of the sample was applied to freshly glow-discharged Quantifoil R 1.2/1.3 400-mesh Au holey carbon grids. Vitrification was as described for the apo structure.

Cryo-EM Data Acquisition. Imaging of ABCD3-apo and ABCD3-phytanoyl-CoA grids was on a Titan Krios 300 keV. microscope. A defocus range of −0.8 to −2.5 was used at a total dose between 45 and 60 e/$Å^2$. The Titan Krios was equipped with a GATAN K3 direct electron detector and a post column energy filter with 20 eV slit width employed during data collection. SerialEM software was used for the data collection with automated data acquisition settings. Data acquisition details including the number of micrographs collected for each dataset, pixel size, dose, are listed in *SI Appendix*, Table S1.

Cryo-EM Image Processing and Model Building. Cryo-EM data processing was performed using cryoSparc as summarized in *SI Appendix*, Figs. S2–S4 (41). Model building of the ABCD3 apo based on the 3.3 Å cryo-EM map used Coot (42). Real space refinement of the structures were performed in PHENIX to obtain the final model (43). ABCD3 apo model was used as a starting point for ABCD3-phytanoyl-CoA and was further fitted and refined in Coot and PHENIX, respectively. PhyCoA SMILES file based on the chemical structure was used to generate restraints in PHENIX eLBOW. The phytanoyl-CoA file from eLBOW was fitted in the cryo-EM density using coot. ABCD3 and phytanoyl-CoA together were refined in PHENIX. ChimeraX was used for visualization and figure preparation (44, 45). The above mentioned software were installed through the SBGrid consortium (46)

Phytanoyl-CoA Binding Analysis. For Microscale thermophoresis (MST) ligand binding experiments (47), purified ABCD3-8xHis protein, expressed in *Sf9* cells, was prepared as described and quantified by measuring absorbance at 280 nm using a NanoOne^C spectrophotometer (Thermo Fisher Scientific). The protein was labeled with Red-tris-NTA dye (NanoTemper) in SEC buffer for 30 min at room temperature. After labeling, the sample was centrifuged at 10,000×*g* for 10 min to remove any protein aggregates. The resulting labeled protein was incubated at 100 nM with varying concentrations of phytanoyl-CoA for 30 min at room temperature. The protein–ligand mixtures were then transferred to premium capillaries (NanoTemper) for analysis using the Monolith NT.115 Pico instrument.

MST measurements were conducted in technical triplicate at 25 °C with medium MST power (40%). Data were analyzed using MO Affinity Analysis software (v3.0.5) to calculate the EC_{50} using Hill fit plot.

Molecular Dynamics Simulation. All-atom molecular dynamics (MD) simulations were performed to investigate the protein and substrate dynamics within a lipid bilayer environment using the GROMACS simulation package (48) and the CHARMM36 force field (49). The MD simulations were initiated using the cryo-EM structure of the phytanoyl-CoA bound ABCD3 protein system. This system was embedded in a pre-equilibrated 1-palmitoyl-2-oleoyl-sn-glycero-3-phosphocholine (POPC) lipid bilayer, generated using the CHARMM-GUI web server (50) and oriented according to the PPM server (51). The system was solvated using the TIP3P water model and neutralized with Na^+ and Cl^- ions to a final concentration of 150 mM, simulating physiological ionic strength. Following 5,000 steps of steepest descent energy minimization, the system underwent a multistage equilibration protocol totaling 50 ns, during which positional restraints on protein heavy atoms and lipid phosphorus atoms were gradually released. An additional 50 ns of unrestrained NPT equilibration ensured thorough system relaxation prior to production simulations.

Three independent production MD simulations, each 500 ns in duration, were performed under the NPT ensemble, maintaining 303.15 K and 1.0 bar using the velocity-rescale thermostat and C-rescale semi-isotropic barostat, respectively. Electrostatic interactions were treated with the Particle Mesh Ewald (PME) method, while van der Waals interactions used a switched cutoff scheme. The LINCS algorithm constrained bonds involving hydrogen atoms, permitting a stable 4 fs integration timestep enabled by hydrogen mass repartitioning (HMR). Using these simulation parameters and settings, system equilibration was confirmed by analyzing membrane thickness and area per lipid over the final 50 ns of the NPT equilibration phase. Structural stability of both protein and ligand during the three independent production runs was subsequently evaluated via RMSD calculations of protein backbone Cα atoms and phytanoyl-CoA heavy atoms (*SI Appendix*, Fig. S5).

Data, Materials, and Software Availability. The Electron Microscopy Data Bank (EMDB) accession codes for cryo-EM density maps are EMD-49388 (52) for apo human ABCD3 and EMD-49386 (53) for phytanoyl-CoA bound human ABCD3, respectively. The structural models are deposited in the Protein Data

Bank (PDB) database under accession codes 9NGM (54) (apo) and 9NGJ (55) (phytanoyl-CoA bound).

ACKNOWLEDGMENTS. We thank Phoung Nguyen and Alisa Bowen for help with initial protein expression trials. We are grateful to Doug Rees and Robert Tampé for their reviews and insightful suggestions. Research was supported by the National Institute on Aging R00AG070271, and American Heart Association 835634 to M.G., National Institute of General Medical Sciences (NIH UC2 HD113474, NIGMS 1R35GM156263-01 to R.M.S, and NIGMS R35GM151256 to I.E.). We are grateful to David Bulkley, Glenn Gilbert, and Matt Harrington for advice with EM data collection carried out at the UCSF cryo-EM facility (supported by NIH Grants S10OD020054, S10OD021741, and S10OD026881). A part of this work was performed at the Stanford-SLAC Cryo-EM Center (S2C2), which is supported by the National Institute of General Medical Sciences (1R24GM154186). The content is solely the responsibility of the authors and does not necessarily represent the official views of the NIH. We thank the following S2C2 personnel for their invaluable support and assistance: Patrick Mitchell, Corey Hecksel, Lydia-Marie Joubert, Megan Mayer, Lisa Dunn. We acknowledge the contributions of the OHSU Biophysics Shared Resource Core (Research Resource ID: RRID: SCR_022744) in facilitating this work.

Author affiliations: [a]Department of Chemical Physiology and Biochemistry, Oregon Health and Science University, Portland, OR 97239; [b]Department of Biochemistry and Biophysics, University of California, San Francisco, CA 94143; [c]Department of Bioengineering and Therapeutic Sciences, University of California San Francisco, CA 94158; and [d]Quantitative Biosciences Institute, University of California, San Francisco, CA 94158

1. A. Baker *et al.*, Peroxisomal ABC transporters: Functions and mechanism. *Biochem. Soc. Trans.* **43**, 959–965 (2015).
2. S. Wilkens, Structure and mechanism of ABC transporters. *F1000Prime Rep.* **7**, 14 (2015).
3. J. Xiong, J. Feng, D. Yuan, J. Zhou, W. Miao, Tracing the structural evolution of eukaryotic ATP binding cassette transporter superfamily. *Sci. Rep.* **5**, 16724 (2015).
4. D. C. Rees, E. Johnson, O. Lewinson, ABC transporters: The power to change. *Nat. Rev. Mol. Cell Biol.* **10**, 218–227 (2009).
5. K. P. Locher, Mechanistic diversity in ATP-binding cassette (ABC) transporters. *Nat. Struct. Mol. Biol.* **23**, 487–493 (2016).
6. C. Thomas, R. Tampe, Structural and mechanistic principles of ABC transporters. *Annu. Rev. Biochem.* **89**, 605–636 (2020).
7. M. Dean, T. Annilo, Evolution of the ATP-binding cassette (ABC) transporter superfamily in vertebrates. *Annu. Rev. Genomics Hum. Genet.* **6**, 123–142 (2005).
8. S. Kemp, F. L. Theodoulou, R. J. Wanders, Mammalian peroxisomal ABC transporters: From endogenous substrates to pathology and clinical significance. *Br. J. Pharmacol.* **164**, 1753–1766 (2011).
9. C. W. van Roermund *et al.*, The human peroxisomal ABC half transporter ALDP functions as a homodimer and accepts acyl-CoA esters. *FASEB J.* **22**, 4201–4208 (2008).
10. M. Morita, T. Imanaka, Peroxisomal ABC transporters: Structure, function and role in disease. *Biochim. Biophys. Acta* **1822**, 1387–1396 (2012).
11. M. Islinger, A. Voelkl, H. D. Fahimi, M. Schrader, The peroxisome: An update on mysteries 2.0. *Histochem. Cell Biol.* **150**, 443–471 (2018).
12. R. J. Wanders, Metabolic functions of peroxisomes in health and disease. *Biochimie* **98**, 36–44 (2014).
13. E. Zalckvar, M. Schuldiner, Beyond rare disorders: A new era for peroxisomal pathophysiology. *Mol. Cell* **82**, 2228–2235 (2022).
14. S. Chornyi, L. IJlst, C. W. T. Roermund, R. J. A. Wanders, H. R. Waterham, Peroxisomal metabolite and cofactor transport in humans. *Front. Cell Dev. Biol.* **8**, 613892 (2020).
15. K. Kawaguchi, M. Morita, ABC transporter subfamily D: Distinct differences in behavior between ABCD1-3 and ABCD4 in subcellular localization, function, and human disease. *Biomed. Res. Int.* **2016**, 6786245 (2016).
16. P. Ranea-Robles *et al.*, The peroxisomal transporter ABCD3 plays a major role in hepatic dicarboxylic fatty acid metabolism and lipid homeostasis. *J. Inherit. Metab. Dis.* **44**, 1419–1433 (2021).
17. S. Ferdinandusse *et al.*, A novel bile acid biosynthesis defect due to a deficiency of peroxisomal ABCD3. *Hum. Mol. Genet.* **24**, 361–370 (2015).
18. J. Gartner, H. Moser, D. Valle, Mutations in the 70K peroxisomal membrane protein gene in Zellweger syndrome. *Nat. Genet.* **1**, 16–23 (1992).
19. X. Deng *et al.*, Whole-exome sequencing identifies novel mutation in intrahepatic cholestasis of pregnancy: A case report and literature review. *Z. Geburtshilfe Neonatol.* **229**, 288–293 (2025), 10.1055/a-2468-5250.
20. A. Cortese *et al.*, A CCG expansion in ABCD3 causes oculopharyngodistal myopathy in individuals of European ancestry. *Nat. Commun.* **15**, 6327 (2024).
21. R. R. Reams *et al.*, Immunohistological analysis of ABCD3 expression in Caucasian and African American prostate tumors. *Biomed. Res. Int.* **2015**, 132981 (2015).
22. Y. Zhang, Y. Zhang, J. Wang, J. Yang, G. Yang, Abnormal expression of ABCD3 is an independent prognostic factor for colorectal cancer. *Oncol. Lett.* **19**, 3567–3577 (2020).
23. J. Yin *et al.*, Peroxisomal membrane protein PMP70 confers drug resistance in colorectal cancer. *Cell Death Dis.* **16**, 293 (2025).
24. Y. Li *et al.*, Structural insights into human ABCD3-mediated peroxisomal acyl-CoA translocation. *Cell Discov.* **10**, 92 (2024).
25. Z. P. Chen *et al.*, Structural basis of substrate recognition and translocation by human very long-chain fatty acid transporter ABCD1. *Nat. Commun.* **13**, 3299 (2022).
26. L. T. M. Le, J. R. Thompson, P. X. Dang, J. Bhandari, A. Alam, Structures of the human peroxisomal fatty acid transporter ABCD1 in a lipid environment. *Commun. Biol.* **5**, 7 (2022).
27. R. Wang, Y. Qin, X. Li, Structural basis of acyl-CoA transport across the peroxisomal membrane by human ABCD1. *Cell Res.* **32**, 214–217 (2022).
28. C. Xiong *et al.*, Structural insights into substrate recognition and translocation of human peroxisomal ABC transporter ALDP. *Signal Transduct. Target. Ther.* **8**, 74 (2023).
29. C. Thomas *et al.*, Structural and functional diversity calls for a new classification of ABC transporters. *FEBS Lett.* **594**, 3767–3775 (2020), 10.1002/1873-3468.13935.
30. G. A. Jansen *et al.*, Phytanoyl-CoA hydroxylase is present in human liver, located in peroxisomes, and deficient in Zellweger syndrome: Direct, unequivocal evidence for the new, revised pathway of phytanic acid alpha-oxidation in humans. *Biochem. Biophys. Res. Commun.* **229**, 205–210 (1996).
31. M. Gupta *et al.*, Structural basis of aquaporin-4 autoantibody binding in neuromyelitis optica. *Sci. Adv.* **11**, eadq7560 (2025).
32. S. Pourmal *et al.*, Structural basis of prostaglandin efflux by MRP4. *Nat. Struct. Mol. Biol.* **31**, 621–632 (2024).
33. Y. Jia *et al.*, Structural and functional insights of the human peroxisomal ABC transporter ALDP. *Elife* **11**, e75039 (2022).
34. A. Noll *et al.*, Crystal structure and mechanistic basis of a functional homolog of the antigen transporter TAP. *Proc. Natl. Acad. Sci. U.S.A.* **114**, E438–E447 (2017).
35. D. Guo *et al.*, Energetics of lipid transport by the ABC transporter MsbA is lipid dependent. *Commun. Biol.* **4**, 1379 (2021).
36. C. Perez, A. R. Mehdipour, G. Hummer, K. P. Locher, Structure of outward-facing PglK and molecular dynamics of lipid-linked oligosaccharide recognition and translocation. *Structure* **27**, 669–678 e665 (2019).
37. A. Siarheyeva, F. J. Sharom, The ABC transporter MsbA interacts with lipid A and amphipathic drugs at different sites. *Biochem. J.* **419**, 317–328 (2009).
38. A. Ward, C. L. Reyes, J. Yu, C. B. Roth, G. Chang, Flexibility in the ABC transporter MsbA: Alternating access with a twist. *Proc. Natl. Acad. Sci. U.S.A.* **104**, 19005–19010 (2007).
39. S. Hofmann *et al.*, Conformation space of a heterodimeric ABC exporter under turnover conditions. *Nature* **571**, 580–583 (2019).
40. E. Stefan, S. Hofmann, R. Tampe, A single power stroke by ATP binding drives substrate translocation in a heterodimeric ABC transporter. *Elife* **9**, e55943 (2020).
41. A. Punjani, J. L. Rubinstein, D. J. Fleet, M. A. Brubaker, CryoSPARC: Algorithms for rapid unsupervised cryo-EM structure determination. *Nat. Methods* **14**, 290–296 (2017).
42. P. Emsley, B. Lohkamp, W. G. Scott, K. Cowtan, Features and development of coot. *Acta Crystallogr. D Biol. Crystallogr.* **66**, 486–501 (2010).
43. P. D. Adams *et al.*, PHENIX: A comprehensive Python-based system for macromolecular structure solution. *Acta Crystallogr. D Biol. Crystallogr.* **66**, 213–221 (2010).
44. T. D. Goddard *et al.*, UCSF chimeraX: Meeting modern challenges in visualization and analysis. *Protein Sci.* **27**, 14–25 (2018).
45. E. C. Meng *et al.*, UCSF ChimeraX: Tools for structure building and analysis. *Protein Sci.* **32**, e4792 (2023).
46. A. Morin *et al.*, Collaboration gets the most out of software. *Elife* **2**, e01456 (2013).
47. S. A. Seidel *et al.*, Microscale thermophoresis quantifies biomolecular interactions under previously challenging conditions. *Methods* **59**, 301–315 (2013).
48. M. J. M. Abraham *et al.*, High performance molecular simulations through multi-level parallelism from laptops to supercomputers. *SoftwareX* **1–2**, 19–25 (2015).
49. J. Huang, A. D. MacKerell Jr., CHARMM36 all-atom additive protein force field: Validation based on comparison to NMR data. *J. Comput. Chem.* **34**, 2135–2145 (2013).
50. J. Lee *et al.*, CHARMM-gui input generator for NAMD, GROMACS, AMBER, OpenMM, and CHARMM/OpenMM simulations using the CHARMM36 additive force field. *J. Chem. Theory Comput.* **12**, 405–413 (2016).
51. A. L. Lomize, S. C. Todd, I. D. Pogozheva, Spatial arrangement of proteins in planar and curved membranes by PPM 3.0. *Protein Sci.* **31**, 209–220 (2022).
52. M. Gupta, N. Khandelwal, R. M. Stroud, "CryoEM structure of human ABCD3." Electron Microscopy Data Bank. https://www.ebi.ac.uk/emdb/EMD-49388. Deposited 26 February 2025.
53. M. Gupta, N. K. Khandelwal, R. M. Stroud, "CryoEM structure of human ABCD3 bound to Phytanoyl-CoA." Electron Microscopy Data Bank. https://www.ebi.ac.uk/emdb/EMD-49386. Deposited 26 February 2025.
54. M. Gupta, N. K. Khandelwal, R. M. Stroud, "CryoEM structure of human ABCD3." Protein Data Bank. https://doi.org/10.2210/pdb9NGM/pdb. Deposited 26 February 2025.
55. M. Gupta, N. K. Khandelwal, R. M. Stroud, "CryoEM structure of human ABCD3 bound to Phytanoyl-CoA." Protein Data Bank. https://doi.org/10.2210/pdb9NGJ/pdb. Deposited 26 February 2025.